

# The Molecular Architecture of Axonemes Revealed by Cryoelectron Tomography

Daniela Nicastro,<sup>1\*†</sup> Cindi Schwartz,<sup>1</sup> Jason Pierson,<sup>1</sup> Richard Gaudette,<sup>1</sup> Mary E. Porter,<sup>2</sup> J. Richard McIntosh<sup>1</sup>

Eukaryotic flagella and cilia are built on a 9 + 2 array of microtubules plus >250 accessory proteins, forming a biological machine called the axoneme. Here we describe the three-dimensional structure of rapidly frozen axonemes from *Chlamydomonas* and sea urchin sperm, using cryoelectron tomography and image processing to focus on the motor enzyme dynein. Our images suggest a model for the way dynein generates force to slide microtubules. They also reveal two dynein linkers that may provide “hard-wiring” to coordinate motor enzyme action, both circumferentially and along the axoneme. Periodic densities were also observed inside doublet microtubules; these may contribute to doublet stability.

Eukaryotic cilia and flagella are built on the axoneme, a cylindrical array of nine doublet microtubules (MTs) that surround two singlet MTs called the central pair (1, 2) (Fig. 1, A and B). Understanding axoneme structure, function, and regulation is important because defects in this organelle are associated with diverse medical problems (3). The motors that transduce chemical energy into the mechanical force for MT sliding are dyneins, large motor enzymes that are organized in two rows along each doublet MT (Figs. 1 and 5, C and D). Other structures in the axoneme resist sliding, causing the axoneme to bend (4). Because

cytoplasmic isoforms of dynein contribute to several forms of MT-based motility (5), and because dynein’s mechanics are distinct from those of the other molecular motors, learning how this enzyme works would be useful.

All dyneins include one or more heavy chains (DHCs, >500 kD each), one or more intermediate chains (DICs, 45 to 140 kD), and 1 to 10 light chains (DLCs, ~8 to 28 kD) (5). The dynein motor domain (~350 kD at the C terminus of the DHC) is related to the AAA family of adenosine triphosphatases. It connects two potential levers: a cargo-binding tail, which is also the binding site of several DICs and

DLCs, and an MT-binding stalk (6). Because flagella generate periodic waves of bending whose speed and form can vary, dynein’s activity probably switches from one side of the axoneme to the other and propagates in a controlled manner (7). Flagellar waveforms seem to result from regulatory and mechanical interactions between projections from the central MTs and the radial spokes (Fig. 1, F and G; Fig. 5, C and D). These structures contain components that modulate kinases and phosphatases on doublet MTs (2). They appear to act through a doublet-associated structure called the dynein regulatory complex (DRC) (1). Given that isolated axonemes are motile (7), it seems likely that all essential regulatory machinery is built into this structure.

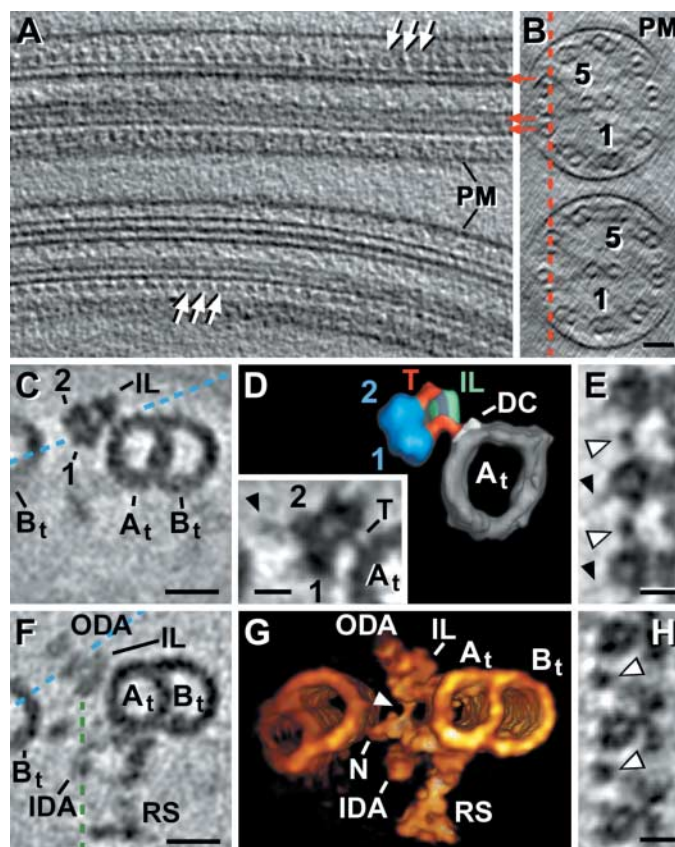
Axonemes from many organisms have been studied by conventional electron microscopy (EM), using thin sections, negative staining, or metal replicas of quickly frozen, deep-etched samples (1, 6, 8). These studies demonstrated the 24-nm axial periodicity of the outer dynein

<sup>1</sup>Laboratory for 3D Electron Microscopy of Cells, Department of Molecular, Cellular, and Developmental Biology, CB 347, University of Colorado, Boulder, CO 80309–0347, USA. <sup>2</sup>Department of Genetics, Cell Biology, and Development, 6–160 Jackson Hall, 321 Church Street SE, University of Minnesota, Minneapolis, MN 55455, USA.

\*Present address: Brandeis University, Rosenstiel, 415 South Street, Waltham, MA 02454, USA.

†To whom correspondence should be addressed. E-mail: nicastro@colorado.edu

**Fig. 1.** Cryo-ET of sea urchin sperm [(A) to (E)] and *Chlamydomonas* flagella [(F) to (H)]. Longitudinal (A) and transverse (B) tomographic slices through flagella are shown; dashed line in (B) indicates the location of (A). (A) Dynein motor domains, white arrows. (B) Top flagellum is viewed from the proximal end; bottom flagellum is opposite, with doublets labeled 1 and 5; PM, plasma membrane. (C), (D), inset in (D), (F), and (G) are cross sections, viewed from the distal end. (C) Slice through an average of 280 repeats; the dashed line defines the orientation of (E). A<sub>v</sub>, A tubule; B<sub>v</sub>, B tubule; IL, DIC/DLC-tail complex; 1 and 2, motor domains of the ODA. (D) Surface rendering of (C) and (D) (inset) with interpretive coloring. The hook-shaped tail (T, red) of the more central DHC connects the dynein head (1, blue area) with A<sub>t</sub>; densities near the A<sub>t</sub> connection resemble the DC (white area). The tail of the peripheral DHC (2, blue area) is obscured by the IL (green area), but relative positions suggest that it is part of the connection to A<sub>t</sub> via the tail of the more central DHC. Note the stalk projecting from 2 toward B<sub>t</sub> (inset, arrowhead). (E) Slice through three ODA motor domains showing stalks (black arrowheads) on motor rings and parts of OOD linkers (white arrowheads). (F) Slice through average of 160 repeats; RS, radial spokes. Dashed blue line, orientation of (H); dashed green line, orientation of Fig. 3, A and B. (G) Volume rendering of (F). Note the nexin link (N) and OID linker (white arrowhead). (H) Slice through three β-dynein motor domains from the ODA row. Note the asymmetric, ring-shaped dynein motors (the middle head is visibly heptameric) and parts of the OOD linker (white arrowheads). Scale bars, 50 nm in (B), 20 nm in (C) and (F), and 10 nm in (D) (inset), (E), and (H).



arms (ODAs) as well as the complex arrangements of the inner dynein arms (IDAs) and radial spokes within the axoneme's 96-nm longitudinal repeat (2, 6) (Fig. 1, A and B; Fig. 5, C and D). We used electron tomography (ET) to study axonemes in rapidly frozen but otherwise unaltered material. Sea urchin sperm were frozen while in a quiescent state (Fig. 1, A to E); axonemes from the biflagellate alga *Chlamydomonas reinhardtii* were isolated and demembrated in the absence of adenosine triphosphate (ATP) (Fig. 1, F to H) (9). Rapid freezing immobilizes samples within milliseconds, raising confidence that the observed structures are accurate representations of physiological states. ET generates three-dimensional (3D) reconstructions with an almost isotropic resolution (10) but through images whose signal-to-noise ratio is low because of the low electron dose that must be used with frozen-hydrated material (11). To get the resolution and contrast necessary to see individual macromolecules, we used an energy filter to remove inelastically scattered electrons (11), correlation-based alignment of equivalent volumes, and 3D volume averaging of repetitive structures, which improves image signal-to-noise ratio [fig. S1, supporting online material (SOM) text, and movie S1] (12). With these methods, image resolution was ~4 nm (fig. S1, G and H), which is sufficient to recognize important molecular details.

**Mechanistic implications of the positions and shapes of dynein arms.** Our images revealed details of dynein's structure in axonemes from both sea urchin (Fig. 1, C to E; Fig. 2, A to D) and *Chlamydomonas* (Fig. 1, F to H; Fig.

2, E and F). A slice through a tomogram that contained the  $\beta$ -dynein heads from three adjacent *Chlamydomonas* ODAs displayed the asymmetry of the dynein motor domain (Fig. 1H): One half of the heptameric ring contained three domains and the other half contained four, which is consistent with images of isolated *Chlamydomonas* IDAs (13), *Dictyostelium* cytoplasmic dynein (14), and sea urchin ODAs (12) (Fig. 1E). The two (sea urchin) or three (*Chlamydomonas*) motor domains in a single ODA formed two or three parallel rings that resembled stacked coins (Fig. 1, C, D, F, and G; Fig. 2, D to F; Fig. 3, A to E; Fig. 5). The plane of each ring ran through the axis of the adjacent B tubule (dashed blue lines in Fig. 1, C and F). Thus, all motor domains were positioned so they could act equivalently on the neighboring MT (Fig. 5C and fig. S4I). The coiled-coil MT-binding stalk probably projects within this plane from the motor domain to the B tubule, although it was often not obvious in our images [but note Fig. 1, D (inset) and E (black arrowheads)]. The ODAs from *Chlamydomonas* [Fig. 1, F to H) and (15)] and sea urchin (Fig. 1, C to E) were similar, suggesting the generality of these relationships and their probable importance for dynein function.

Averages of sea urchin ODAs revealed the tail region of DHCs in situ (Fig. 1, C and D); the tail of the more central DHC was obvious, whereas that of the more peripheral DHC was partially obscured by additional density [Fig. 1, C and D (inset)]. The accessory subunits (the DIC/DLC complex) probably lie near the site where the two tails meet (Fig. 5A). Only the

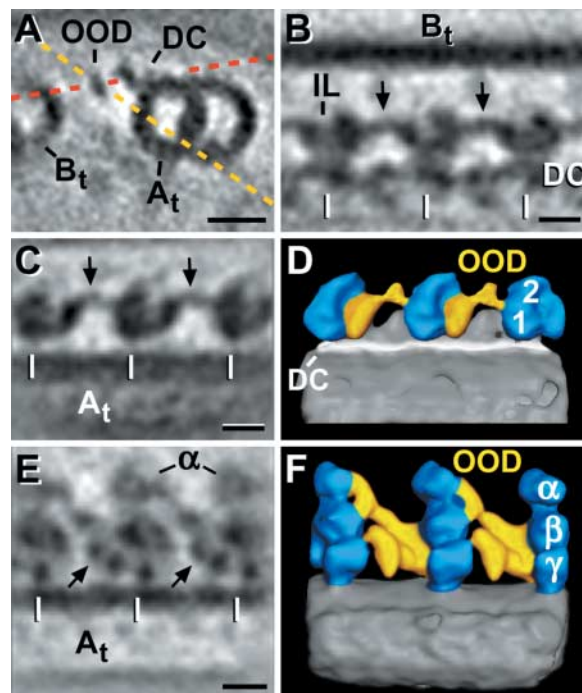
inner  $\alpha$ -DHC connected directly to the A tubule; the  $\beta$ -DHC was carried in a piggyback fashion (Fig. 1D) (12). The tails of the *Chlamydomonas* outer-arm DHCs were less obvious but still visible (IL in Fig. 1, F and G).

ODAs bind the A tubule through the outer-arm docking complex (DC) (16). The DC forms a small pointed structure on the A tubule at the base of the ODA (16) (Figs. 1D and 2A). Two of the DC subunits are elongated polypeptides, which are thought to join end-to-end at every 24-nm interval and form an extended filament along the A tubule. Tomographic slices through the base of the ODAs (red line in Fig. 2A) revealed a narrow density on the surface of the A tubule (Fig. 2B) that corresponds to the predicted location of the DC.

**Orientations of ODA domains in situ modify existing models for dynein's force production.** Sea urchin ODA tails appeared hook-shaped (Fig. 1, C and D), like the EM images of the single-headed IDA isoform "c" from *Chlamydomonas* (13). Images of dynein c have suggested a rotary motion in dynein's head that shifts the coplanar stalk and/or tail relative to the AAA subdomains (13, 14), indicating that the head acts as a winch (17). However, the ODA motor and tail in situ displayed a different 3D orientation, suggesting an alternative interpretation. In axonemes, the ODA tail bent in a plane perpendicular to that of the dynein rings (Fig. 1, C to H). This difference from the planarity seen in vitro (13) could result either from isoform differences or from rearrangements during isolation and/or negative staining. Tail and motor domains were both clearly resolved in our averages; moreover, each ODA formed multiple connections, both along and perpendicular to the axoneme axis (Fig. 5, A and B, and movie S2). These structures may provide rigidity, allowing the tail to serve as a fulcrum for dynein's power stroke. In contrast, the ATP-sensitive MT-binding stalks that connect to B tubules were often smeared under our conditions (Fig. 1). Apparently the tails were essentially static relative to the motor ring and A tubule, whereas the stalk's position was variable. Thus, any rotation of the dynein motor that promotes doublet sliding should cause the MT-binding stalk to shift relative to the more rigid tail.

**Links between dynein complexes may coordinate dynein activity in axonemes.** Tomographic slices that contained a row of ODAs (red and yellow lines in Fig. 2A) showed neighboring arms linked by filamentous structures (Fig. 2, B to F). The orientation and position of these linkers relative to the ODA motor domains showed that they were distinct from the DIC/DLC-tail complex (Fig. 2B; white arrowheads in Fig. 1, E and H). These structures were modeled in 3D as the outer-outer-dynein (OOD) linkers (Fig. 2, D and F; Fig. 5, B and D). In sea urchin sperm, these linkers ran from the ODA motor domain nearest the A tubule,

**Fig. 2.** ODA complexes of sea urchin sperm flagella (A to D) and *Chlamydomonas* axonemes (E and F). A cross-sectional view from the distal end (A) and longitudinal views [(B) to (F)] with the proximal end at left are shown. (A) Slice through an average of 280 doublets. The slice orientation is similar to that in Fig. 1C, but the position is between two ODAs, showing a cross section of an OOD linker. Dashed red line, orientation of slice in (B); dashed yellow line, orientation of slice in (C). Slices [(B), (C), and (E)] and surface renderings [(D) and (F)] show three ODAs, connected by OOD linkers (arrows or yellow areas); two-headed sea urchin ODAs [(blue area labeled 1 and 2 in (D))]; or three-headed *Chlamydomonas* ODAs [blue area labeled  $\alpha$ ,  $\beta$ , and  $\gamma$  in (F)]. White lines in (B), (C), and (E) indicate the 24-nm repeat of ODAs; (D) and (F) correspond to (C) and (E). Both kinds of axonemes have OOD linkers, but sea urchin linkers are almost parallel to the MTs [(B) to (D)], whereas *Chlamydomonas* links are diagonal [(E) and (F)]. Scale bars, 20 nm in (A) and 10 nm in (B), (C), and (E).



up and over to the peripheral motor domain of the neighboring ODA (Fig. 2, C and D; Fig. 5B). In *Chlamydomonas*, the OOD linkers were even larger and more complex (Fig. 2, E and F; Fig. 5D; and fig. S4, D and E). The point of attachment between the OOD linker and the ODAs lay close to the base of the motor domain where the dynein tail begins.

Given the size of these OOD linkers, we re-examined published images, seeking similar densities. Although there are ambiguities in such comparisons (6, 8, 18) (fig. S4, D and E), similar structures could be seen in previous work. Burgess's intermediate subunit (18) resembles our sea urchin OOD linker [compare Fig. 2C with figure 6D in (18)]. The diagonal component in *Chlamydomonas* may be our OOD linker [Fig. 2E versus figure 9 in (19)]. The presence of linkers in such distantly related species suggests that they are ubiquitous axonemal features. These linkers are ideally positioned to modulate dynein activity along outer doublets during flagellar waveform propagation.

We also found connections between OOD linkers in the outer arms and structures in the IDA region (Fig. 3, A to E; white arrowhead, Fig. 1G). In each 96-nm repeat, two of the four OOD linkers connected to the IDA region, forming part of a triskelion; one connection was proximal to the first radial spoke, whereas the other was distal to the second spoke (black arrows, Fig. 3, A to C, and movie S3). These connections are outer-inner-dynein (OID) linkers (Fig. 5D). The proximal OID linker connected with the base of an IDA called I1 (Fig. 3, A and C), whereas the second OID linker connected with the DRC, a crescent-shaped structure above the second radial spoke (20, 21) (Figs. 1G and 3, A to E). The OID linkers suggest a mechanism for coordinating inner and outer dynein arm activities: Signals from the central pair and radial spokes are transmitted first to the I1 dynein and DRC to generate flagellar waveforms. From there, the signals may go through OID linkers to the ODAs to modulate flagellar beat frequency. This model is consistent with observations from flagellar

mutants and indicates that ODAs are downstream on the signaling pathway (22).

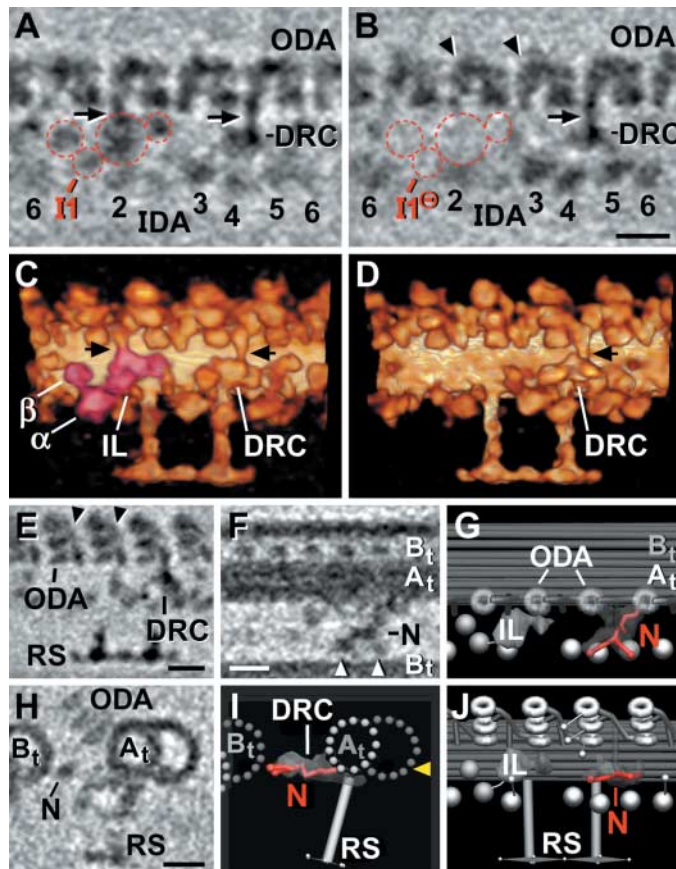
**IDA organization in *Chlamydomonas axonemes*.** IDAs are structurally and functionally more complex than ODAs, and they are both necessary and sufficient for generating the diversity of flagellar waveforms (22). In *Chlamydomonas*, at least eight different inner-arm DHCs are organized with various DICs and DLCs into seven distinct complexes: one two-headed dynein (I1) and six single-headed isoforms (22). We observed the IDAs in 3D within the 96-nm axoneme repeat (Fig. 3, A to E) (6, 20, 21). The reproducibility and sensitivity of our methods were revealed by comparisons between wild-type axonemes and a previously characterized IDA mutant (*pf9-3*) (23) that fails to assemble the I1 dynein (fig. S2). Tomographic slices through this region in wild-type axonemes revealed at least three densities: the two I1 motor domains and the DIC/DLC complex (Fig. 3, A and C; Fig. 5D; fig. S2, B to F; movies S3 and S5) missing in the *pf9-3* mutant (Fig. 3, B and D; fig. S2, G to K; movies S4 and S5). The DIC/DLC complex of I1 (6, 20, 21) made contact with neighboring structures in both ODA and IDA regions (Fig. 3, A and C; Fig. 5D). One of these contacts corresponded to the proximal OID linker, which is consistent with known interactions between ODA components and the I1 subunits DIC138 and DLC7b (24).

ET of the IDAs identified five additional globular domains per 96-nm repeat; these domains lay in the same row as one of the I1 motor domains and were of comparable size (Fig. 1G; Fig. 3, A to E; Fig. 5, C and D; fig. S4, E, H, and I; movie S6). We interpret such densities as the motor domains of five single-headed IDAs (Fig. 3, A to D; Fig. 5D). The IDAs appeared attached to the A tubule by long tails (fig. S4, F to H); several of these inserted close to the base of both radial spokes and/or below the DRC, which is consistent with the failure of certain IDAs to assemble in DRC mutants (21, 25).

Each of the IDA and ODA motor domains was situated with its surface ~12 nm from the adjacent B tubule (Fig. 5C and fig. S4I). This distance is consistent with the length of the MT-binding stalk that projects from isolated dynein motor domains (17), suggesting that all of these dyneins could interact with the B tubule and contribute to force production. MT-binding stalks were visible in only a few averages [Fig. 1, D and E; movie S2], suggesting that their positions were variable, as one would expect for structures that adopt various conformations.

**The nexin link associates with the dynein regulatory complex.** Nexin was identified in early EM of axonemes (4) as a flexible protein that connects neighboring doublet MTs (Fig. 1G; Fig. 3, F to J; fig. S3) (6, 26, 27). Nexin is thought to contribute elastic resistance that converts doublet sliding into axoneme bending (4, 26). In our images, one end of the *Chlamy-*

**Fig. 3.** Organization of IDAs (A to E) and nexin link (F to J) in *Chlamydomonas* axonemes. Wild-type [(A) and (C)] and *pf9* mutant [(B), (D), and (E)] axonemes show clear differences. Longitudinal slices [(A), (B), and (E)] and volume renderings [(C) and (D)] are viewed from the B tubule of the adjacent doublet, with the proximal end on the left; the orientation of (A) and (B) is indicated by the dashed green line in Fig. 1F; (C) and (D) correspond to (A) and (B). The I1 complex (dashed red circles or red areas) is missing in the mutant (*I1*<sup>-</sup>). Note the OID linkers (arrows) between the ODA and IDA rows. Arrowheads, OOD linkers;  $\alpha$  and  $\beta$ , 1-alpha and 1-beta motor domains of the I1 complex; 2 to 6, single-headed IDAs. (E) Similar to (B) but oriented to include all three ODA motor domains and radial spoke heads (RS); OOD linkers (arrowheads) connect to  $\alpha$ - and perhaps  $\beta$ -DHCs on their proximal sides, whereas in (B) the OOD linkers connect to  $\beta$ - and  $\gamma$ -DHCs on their distal sides. Slices [(F) and (H)] through an average of 160 nexin links (N) and graphic models [(G), (I), and (J)] of the same structure; the orientations of (G) and (I) correspond to (F) and (H). Nexin spans the distance between A and B tubules of adjacent doublets; it is connected to the DRC. It terminates on the A tubule close to RS2, but branches near the B tubule [arrowheads in (F) at tips of the branches]. Nexin zigzags between the A tubule and the bifurcation point. (F) is a longitudinal slice at the position of the yellow arrowhead in (I). Scale bars, 20 nm [(B), (E), (F), and (H)].



*ylomonas* nexin formed a bifurcated attachment to the B tubule (Fig. 3, F, G, and J; fig. S3, A and B); the other was attached to the A tubule close to the base of the second radial spoke, adjacent to the DRC (Fig. 3, F, G, I, and J; fig. S3, D to G).

The crescent-shaped density of the DRC made contact with both ODAs and IDAs, as well as with radial spoke 2 (Figs. 3 and 5, C and D). A considerable fraction of the mass connected with the DRC extended some nanometers from the surface of the A tubule (Figs. 3I and 5C; movies S3 to S6). Indeed, nexin appeared to form a major part of the DRC (20, 26). These images support a model in which the DRC and nexin interact with and mediate regulatory signals between the radial spokes and both inner and outer dynein arms (20, 21, 26).

The axonemes we studied were more or less straight, but even so nexin was longer (~40 nm) than the shortest distance between adjacent doublets (~30 nm) (Fig. 3F and fig. S3, A to E). Moreover, the part of the link that connected the A-MT anchor and B-MT bifurcation point appeared as a zigzag structure (Fig. 3, F, G, and I; fig. S3, A to E). This configuration may provide a reservoir of folded protein that could contribute to both the overall length extension and to the elastic restoring force that nexin is thought to provide for doublet MT sliding.

**Structures on the inner surfaces of doublet microtubules might increase their stability.** Doublet MTs are notable for both their unusual architecture and their stability as compared with cytoplasmic MTs. The A tubule was a complete cylinder of 13 protofilaments (A1 to A13), but the B tubule contained only 11 filaments (B1 to B11), one of which (B11) looked

thinner than the others (Fig. 1, C and F; Fig. 4, D, E, H, and I) (28). The A tubule appeared slightly oval in cross sections (Fig. 1, C and F; Figs. 2A and 4D). Many proteins associate with the outer surfaces of doublet MTs, but we did not expect to find periodic densities on the inner surfaces of A and B tubules in both sea urchin (Fig. 4, G to I) and *Chlamydomonas* axonemes (Fig. 4, A

to F; fig. S2, D to F and I to K). Averages of 96-nm repeats revealed three MT inner proteins (MIPs) that differed in location, size, and periodicity. MIP1 was the smallest. It lay next to protofilament A5 and showed 8-nm periodicity along the MT axis [Fig. 4, A, D, G, and H; purple dot in Fig. 4, E and F, and Fig. 5C]. MIP2 was larger, was positioned between protofilaments

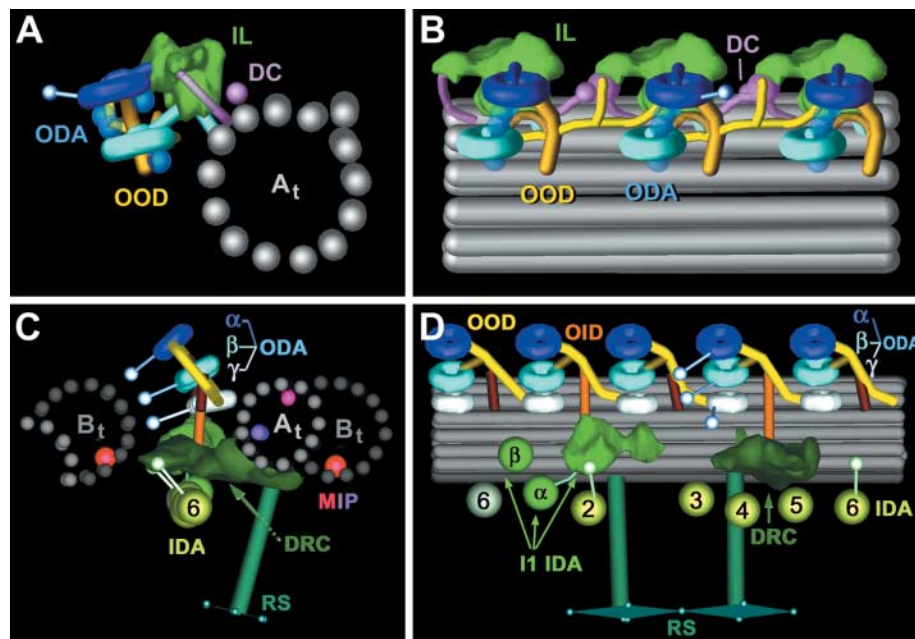
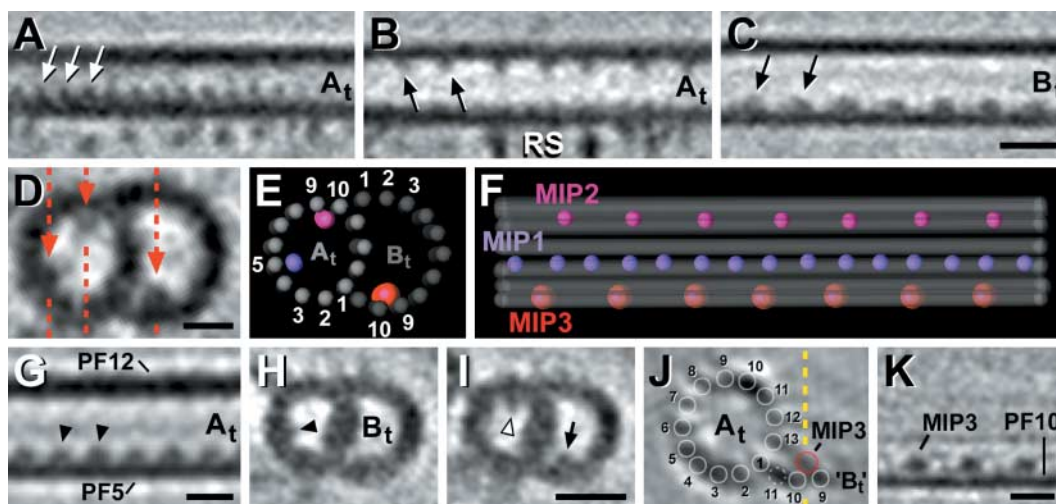


**Fig. 5.** Summarizing models of the ODA row in the sea urchin sperm flagellum (A and B) and the 96-nm repeat in *Chlamydomonas* axonemes (C and D). (A) and (C) are viewed from the distal end; in (B) and (D), the proximal end is at left. (A) and (B) show the ODA row, the OOD linker (yellow), IL (green), DC (pink), and additional densities surrounding the dynein motor domains (blue). These seem to form supporting structures around the ODA complexes. [(C) and (D)] MT-associated structures in *Chlamydomonas* axonemes.  $\alpha$  and  $\beta$ , 1-alpha and 1-beta DHC of the I1 complex; 2 to 6, single-headed IDAs; alpha ( $\alpha$ ), beta ( $\beta$ ), and gamma ( $\gamma$ )-ODA, DHCs of the ODAs; OID linker (orange area); OOD linker (yellow area).

**Fig. 4.** MIPs in sea urchin sperm [(G) and (I)] and *Chlamydomonas* axonemes [(A) to (F), (J), and (K)]. In longitudinal views [(A) to (C), (F), (G), and (K)], the proximal end is at left; in cross sections [(D), (E), and (H) to (J)], the view is from the distal end. (A to D) Slices of MT doublets showing periodic densities attached to the inner MT wall (arrows). Dashed lines in (D) indicate the positions of the slices depicted in [(A), MIP1], [(B), MIP2], and [(C), MIP3]. The MIPs show 8-nm [white arrows in (A)] or 16-nm [black arrows in (B) and (C)] periodicities, respectively. (E and F) Graphic model of a 96-nm repeat showing MIPs (purple, MIP1; pink, MIP2; red, MIP3) relative to the protofilaments (numbered) of  $A_t$  and  $B_t$ . (G to I) MIP1 [black arrowheads in (G) and (H)], MIP2 [white arrowhead in (I)], and MIP3 [black arrow in (I)] in outer doublets of sea urchin sperm flagella. (J and K) MT doublet with protofilaments 1 to 13 of  $A_t$ , but only protofilaments 9 to 11 of the  $B_t$  tubule. MIP3 is still present, suggesting that it may enhance the stability of protofilaments 9 to 11 of this tubule. The dotted yellow line in (J)



indicates the orientation of the slice in (K). The image quality of the partial doublet is lower than that of other averages because there were no other doublets with similar protofilament losses at other orientations relative to the missing wedge to help compensate for the missing information; the anisotropy of the resolution is obvious, especially along the z axis [horizontal in (J)]. Scale bars, 20 nm in (C) and (I) and 10 nm in (D), (G), and (K).

A9 and A10, and showed 16-nm periodicity [Fig. 4, B, D, and I; pink dot in Fig. 4 (E and F) and Fig. 5C]. MIP3 was the largest and lay between protofilaments B9 and B10 with 16 nm-periodicity [Fig. 4, C, D, and I; red dot in Fig. 4, E and F, and Fig. 5C]. The MIPs were present in all outer doublets and in both sea urchin (Fig. 4, G to I) and *Chlamydomonas* (Fig. 4, A to F), suggesting that they are universal features of axonemes. Although material has previously been seen in the lumen of doublets from insect and human sperm (29), MIPs have not been recognized as a consistent, periodic feature of outer doublets. Images of homogenized, high salt-extracted sea urchin sperm flagella also revealed features inside doublet MTs (30), but this study was limited by nonphysiological conditions and by the anisotropic resolution that is characteristic of single-axis tomography (fig. S1).

Doublet MTs treated with increasing concentrations of ionic detergents dissolve in a defined sequence: first the outer portion of the B tubule, then the rest of the B tubule, followed by the outer portion of the A tubule and then the remainder of the A tubule, leaving a ribbon of three protofilaments (31). Our axonemes were incubated in physiological buffers, but occasionally they contained a few partially dissolved doublets that were consistent with this pattern of disintegration. In one example, the A tubule was intact, but only protofilaments B9 to B11 remained; these still bound MIP3 (Fig. 4, J and K), suggesting that MIPs give structural stability to MTs protofilaments. Several small ligands, such as Taxol, interact with the luminal side of the MT wall and affect polymer stability (32). Perhaps MIPs alter doublet stability in a similar way. Doublet stability may also be affected by the especially robust ribbon of three protofilaments that

include tubulin, tektin, and several tightly associated proteins (28). Tektin may also associate with the DRC and IDAs (33). Notably, MIP1 was in the A tubule close to the DRC, and MIP3 was in the B tubule near the attachment of nexin (Fig. 5C). Perhaps the MIPs provide structural reinforcement at sites of mechanical stress and information transfer. The further characterization of these proteins may provide valuable physiological and therapeutic insights.

Future comparisons between wild-type and mutant axonemes should help to define the function of additional components in the axoneme. Work on mutant axonemes from human patients may also help to clarify the underlying causes of diseases related to flagellar and ciliary dysfunction. Given the complexity of axoneme structure and the biological importance of its many functions, cryo-ET is likely to play a major role in clarifying both the normal and abnormal mechanisms of this conserved biological machine.

#### References and Notes

1. M. E. Porter, W. S. Sale, *J. Cell Biol.* **151**, F37 (2000).
2. E. F. Smith, P. Yang, *Cell Motil. Cytoskeleton* **57**, 8 (2004).
3. J. Pan, Q. Wang, W. J. Snell, *Lab. Invest.* **85**, 452 (2005).
4. G. B. Witman, J. Plummer, G. Sander, *J. Cell Biol.* **76**, 729 (1978).
5. M. Sakato, S. M. King, *J. Struct. Biol.* **146**, 58 (2004).
6. U. W. Goodenough, J. E. Heuser, *Structure of the Soluble and in Situ Ciliary Dyneins Visualized by Quick-Freeze Deep-Etch Microscopy*, vol. 1 of *Cell Movement*, F. P. Warner, Ed. (Liss, New York, 1989).
7. I. R. Gibbons, *J. Cell Biol.* **91**, 107s (1981).
8. P. Lupetti *et al.*, *Cell Motil. Cytoskeleton* **62**, 69 (2005).
9. Materials and methods are available as supporting material on Science Online.
10. J. Frank, *Electron Tomography: Three-Dimensional Imaging with the Transmission Electron Microscope* (Plenum, New York, 1992).
11. A. J. Koster *et al.*, *J. Struct. Biol.* **120**, 276 (1997).
12. D. Nicastro, J. R. McIntosh, W. Baumeister, *Proc. Natl. Acad. Sci. U.S.A.* **102**, 15889 (2005).

13. S. A. Burgess, M. L. Walker, H. Sakakibara, P. J. Knight, K. Oiwa, *Nature* **421**, 715 (2003).
  14. M. P. Koonce, M. Sams, *Trends Cell Biol.* **14**, 612 (2004).
  15. H. Sakakibara, S. Takada, S. M. King, G. B. Witman, R. Kamiya, *J. Cell Biol.* **122**, 653 (1993).
  16. S. Takada, R. Kamiya, *J. Cell Biol.* **126**, 737 (1994).
  17. S. A. Burgess, P. J. Knight, *Curr. Opin. Struct. Biol.* **14**, 138 (2004).
  18. S. A. Burgess, S. D. Dover, D. M. Woolley, *J. Cell Sci.* **98**, 17 (1991).
  19. G. B. Witman, N. Minervini, *Symp. Soc. Exp. Biol.* **35**, 203 (1982).
  20. D. N. Mastronarde, E. T. O'Toole, K. L. McDonald, J. R. McIntosh, M. E. Porter, *J. Cell Biol.* **118**, 1145 (1992).
  21. L. C. Gardner, E. O'Toole, C. A. Perrone, T. Giddings, M. E. Porter, *J. Cell Biol.* **127**, 1311 (1994).
  22. R. Kamiya, *Int. Rev. Cytol.* **219**, 115 (2002).
  23. S. H. Myster, J. A. Knott, E. O'Toole, M. E. Porter, *Mol. Biol. Cell* **8**, 607 (1997).
  24. L. M. DiBella *et al.*, *Mol. Biol. Cell* **15**, 4633 (2004).
  25. G. Piperno, K. Mead, M. LeDizet, A. Moscatelli, *J. Cell Biol.* **125**, 1109 (1994).
  26. D. M. Woolley, *J. Cell Sci.* **110**, 85 (1997).
  27. C. B. Lindemann, L. J. Macauley, K. A. Lesich, *Biophys. J.* **89**, 1165 (2005).
  28. D. Nojima, R. W. Linck, E. H. Egelman, *Curr. Biol.* **5**, 158 (1995).
  29. B. A. Afzelius, R. Dallai, S. Lanzavecchia, P. L. Bellon, *Tissue Cell* **27**, 241 (1995).
  30. H. Sui, K. H. Downing, *Nature*, **442**, 475 (2006).
  31. G. B. Witman, K. Carlson, J. Berliner, J. L. Rosenbaum, *J. Cell Biol.* **54**, 507 (1972).
  32. K. H. Downing, *Annu. Rev. Cell Dev. Biol.* **16**, 89 (2000).
  33. H. A. Yanagisawa, R. Kamiya, *Mol. Biol. Cell* **15**, 2105 (2004).
34. We thank R. Linck for helpful discussions, D. Mastronarde for help with image processing, and the National Center for Research Resources (grant RR 000592 to J.R.M.) and NIH (grant 2R37-GM55667 to M.E.P.) for financial support.

#### Supporting Online Material

www.sciencemag.org/cgi/content/full/313/5789/944/DC1  
Materials and Methods

SOM Text

Figs. S1 to S4

References

Movies S1 to S6

11 April 2006; accepted 5 July 2006

10.1126/science.1128618

## REPORTS

# Electronically Induced Atom Motion in Engineered CoCu<sub>n</sub> Nanostructures

Joseph A. Stroschio,<sup>1\*</sup> Francesca Tavazza,<sup>2</sup> Jason N. Crain,<sup>1</sup> Robert J. Celotta,<sup>1</sup> Anne M. Chaka<sup>2</sup>

We have measured the quantum yield for exciting the motion of a single Co atom in CoCu<sub>n</sub> linear molecules constructed on a Cu(111) surface. The Co atom switched between two lattice positions during electron excitation from the tip of a scanning tunneling microscope. The tip location with highest probability for inducing motion was consistent with the position of an active state identified through electronic structure calculations. Atom motion within the molecule decreased with increased molecular length and reflected the corresponding variation in electronic structure.

Atom manipulation with the scanning tunneling microscope (STM) is accomplished by using a tunable chemical bond between the adatom and the scanning tip and/or local electronic excitations via the tun-

ing electrons (1–3). The dynamics of atomic motion during such processes can be followed by analyzing the noise in the tunneling signal (4, 5). Such atomic motion is ultimately controlled by both the energy landscape and the

type of excitation and relaxation pathways the atoms encounter, as revealed by recent tunneling noise spectroscopy studies for single atoms and small molecules (6–11). Through clever design of molecular configurations, energy barriers can be engineered to facilitate long-range motion in larger molecular nanostructures (12).

In this report, we demonstrate that motion of a single atom within a larger nanostructure can be induced by using electron excitation mechanisms in the STM. The use of tunneling noise spectroscopy measurements, together with den-

<sup>1</sup>Center for Nanoscale Science and Technology, <sup>2</sup>Chemical Science and Technology Laboratory, National Institute of Standards and Technology, Gaithersburg, MD 20899–8412, USA.

\*To whom correspondence should be addressed. E-mail: joseph.stroschio@nist.gov